

This is the accepted manuscript made available via CHORUS. The article has been published as:

# Valley contrasting in epitaxial growth of In/Tl homoatomic monolayer with anomalous Nernst conductance

Jian Zhou, Chengxi Huang, Erjun Kan, and Puru Jena

Phys. Rev. B **94**, 035151 — Published 25 July 2016

DOI: [10.1103/PhysRevB.94.035151](https://doi.org/10.1103/PhysRevB.94.035151)

# Valley contrasting in epitaxial growth of In/Tl homoatomic monolayer with anomalous Nernst conductance

Jian Zhou<sup>1,\*</sup>, Chengxi Huang<sup>2,1</sup>, Erjun Kan<sup>2</sup>, Puru Jena<sup>1</sup>

<sup>1</sup>*Physics Department, Virginia Commonwealth University, Richmond, Virginia 23284, United States*

<sup>2</sup>*Department of Applied Physics and Key Laboratory of Soft Chemistry and Functional Materials (Ministry of Education), Nanjing University of Science and Technology, Nanjing, Jiangsu 210094, P. R. China*

## Abstract

Over the past few years various valleytronic properties have been predicted in graphene-like  $p$ -electron honeycomb structures with staggered sublattice on-site potential. However, most of these studies are based on model calculations and direct studies on real materials are still rare. In this work, we propose an experimentally feasible structure based on an epitaxial growth of In/Tl honeycomb lattice on a semi-hydrogenated graphene/diamond thin film substrate. Our first-principles calculations reveal that due to different absorption sites of the two In/Tl sublattices, the inversion symmetry and quasi-2D inversion symmetry are broken, yielding inequivalent band gaps at the  $K$  and  $K'$  points of the Brillouin zone. In addition, compared with previous graphene-based models, In/Tl also has a large spin-orbit coupling (SOC). In this regard, such a  $p$ -electron based system is a good candidate for valley selective circular polarization light absorption. Simultaneously, by integrating its Berry curvatures, we reveal a large SOC induced anomalous Nernst effect, which supports a pure spin current at its Fermi level.

PACS: 63.22.-m, 73.20.Hb, 71.70.Ej, 11.30.Qc

---

\* jzhou2@vcu.edu

## I. Introduction

The discovery of two-dimensional (2D) transition metal dichalcogenide (TMD) has given rise to immense interest in valley contrasting physics and its potential applications [1,2]. Valley is viewed as a novel degree of freedom of an electron, in addition to its charge and spin. In a honeycomb lattice, the two valleys can locate at the corner of the first Brillouin zone (BZ), well separated with weak inter-valley interactions. When the structure lacks inversion symmetry, these two valleys become inequivalent and the valley excitations are contrasting [3]. Electrons in different valleys can then be selectively excited by different circularly polarized light. This leads to possible realization of valleytronics, providing an opportunity for an effective control of quantum computing and optoelectronics. Consequently, the search and design of valleytronic materials is an active field.

Currently there are two main categories of proposed valleytronic materials. One belongs to the family of TMD monolayers such as  $H\text{-MoS}_2$ , whose valence and conduction bands are mainly contributed by Mo- $d$  electrons, mixed with small portion of S- $p_{x,y}$  electrons. The contrasting valley behavior comes due to the breaking of inversion symmetry and inclusion of large spin-orbit coupling (SOC) interaction [4]. The other family is based on  $p$ -electron homoatomic honeycomb materials with staggered sub-lattice on-site potential (the on-site energy difference is denoted as  $\Delta$ ) [5-10]. The  $p$ -electron spintronics is advantageous over the conventional  $d$ - or  $f$ -electron based magnetic systems due to long electron spin coherence time. Such staggered potential breaks the inversion symmetry and opens a band gap at the corner of the first BZ. Up to now most studies in this family are based on model calculations and limited to graphene monolayer which has small SOC. In reality, a substrate is required to introduce such staggered potential into honeycomb lattice. How to select a suitable substrate has not been well discussed and remains an open question. In addition, the marginal SOC interaction of graphene-based systems hinders their potential applications. In this regard, finding realizable homoatomic honeycomb structures composed of heavy  $p$ -electron atoms with an appropriate substrate is important for developing new valleytronic devices.

This is not easy because the adsorbed honeycomb layer should have small lattice mismatch with the substrate, and the whole system has to be dynamically stable and experimentally feasible. Furthermore, the substrate has to open a large bulk band gap around the

Fermi level, hence the low energy bands are mainly contributed by the adsorbed honeycomb layer. The optimal adsorption pattern of the honeycomb layer has to possess quasi-2D inversion asymmetry, so that it opens a direct band gap, rather than forming a Dirac point at the Fermi level [11]. Here, we propose a possible route to realize valley contrasting properties in a feasible  $p$ -electron based homoatomic honeycomb lattice composed of heavy atoms. By using first-principles calculations we predict a stable valley contrasting honeycomb ( $h$ -) indium (or thallium) monolayer supported on a semi-hydrogenated graphene. Such semi-hydrogenated graphene sheet (referred to as graphone) was first predicted theoretically [12, 13] and later successfully fabricated in experiments [14]. The  $h$ -In/Tl monolayer can then be experimentally fabricated by molecular beam epitaxial or chemical vapor deposition technique. We denote the saturated C atoms as C1, and the unsaturated atoms as C2. We find that in the ground state, one sub-lattice of  $h$ -In resides on the C1 site, while the other sub-lattice of  $h$ -In prefers the C2 site. In this way, the graphone substrate provides a staggered sub-lattice on-site potential for  $h$ -In monolayer, and the quasi-2D inversion symmetry is broken. While the isolated  $h$ -In monolayer is dynamically unstable, the graphone substrate stabilizes it according to our phonon dispersion calculation. Band structure calculation based on generalized gradient approximation (GGA) further reveals a direct band gap of 46 meV at the  $K$  point of the BZ, and hybrid functional treatment of exchange-correlation potential validates this direct band gap with a value of 176 meV. Both valence and conduction bands are located inside the band gap of the graphone substrate. Due to the breaking of inversion symmetry, the valleys of  $h$ -In monolayer become inequivalent. The SOC interaction induces an obvious Rashba type band splitting; hence, this material exhibits ideal Rashba states that are well separated from substrate bands [15]. The spin texture of conduction band shows a clear hedgehog skyrmion pair around the  $K$  and  $K'$  valley. We also reveal a valley selective phenomenon for inter-band transitions at  $K$  and  $K'$  points. Furthermore, by integrating Berry curvatures we observe a large anomalous Nernst effect at room temperature and a pure spin current can be generated by a thermal gradient. The substrate thickness effect is also discussed. Similar Rashba effect can be observed in  $h$ -Tl monolayer on graphone.

## II. Computational Details

The first-principles calculations are based on density functional theory as implemented in the Vienna *ab initio* simulation package (VASP) [16]. We use GGA to treat the exchange-correlation potential in the form proposed by Perdew, Burke, and Enzerhof (PBE) [17]. The core electrons are treated by projector-augmented wave method [18], and a planewave basis set is used to describe valence electrons. The cutoff energy is set to be 520 eV. The simulation supercell contains a (2×2) graphone substrate (eight C atoms and four H atoms) and two In atoms, with a small lattice mismatch. Vacuum space of 18 Å is applied along the  $z$  direction to avoid interactions between different image layers. Following a convergence test, a  $\Gamma$ -centered (9×9×1) Monkhorst-Pack  $k$ -point mesh [19] is used to represent the reciprocal space for optimizing the geometry and calculating the electronic property. In order to calculate the Nernst conductivity coefficients, we integrate Berry curvatures in the whole 2D BZ. The integration is performed on a fine  $k$ -point mesh. We use a (90×90×1)  $k$ -mesh to represent the region having almost constant Berry curvatures, and a much denser  $k$ -mesh equivalent to (450×450×1) is applied when the Berry curvatures change dramatically. We use conjugated gradient method to optimize the structure without any symmetry constraint. The convergence criteria of total energy and force components are set to be  $1 \times 10^{-4}$  eV and 0.01 eV/Å, respectively. The phonon dispersions are calculated using the density functional perturbation theory (DFPT) method implemented in the Phonopy code [20].

### III. Results

#### A. Electron counting consideration of adsorbing layer

The reason for selecting group-IIIA elements In/Tl is based on the following electron counting analysis. By evaluating the atomic radii of  $5p$  and  $6p$  elements, we found that a (2×2) graphone sheet (thinnest diamond (111) film) would have small lattice mismatch to support a honeycomb structure composed of two heavy atoms in the simulation supercell. In each supercell of a (2×2) graphone, there are four exposed C- $p_z$  orbitals that need to be saturated so that the magnetism of graphone substrate can be totally quenched. Therefore, four electrons are needed from the heavy atoms. In addition, each heavy atom needs one electron to form valence bands. Hence, each heavy element should contain  $(4/2+1) = 3$  valence electrons. This requires a group-IIIA element, i.e. In or Tl in the  $5p$  and  $6p$  blocks, respectively. In this case, all dangling bonds

of C atoms are saturated and a large band gap appears in their projected band structure. Hence, the  $h$ -In/Tl lattice would show valence and conduction bands in the gap of substrate C, with band extrema (valence band maximum, VBM; conduction band minimum, CBM) appearing at  $K$  and  $K'$  points of the BZ. Our numerical results in the following confirm these analyses.

## B. Geometric structure and dynamical stability

In Figure 1(a) we show the structure of  $h$ -In monolayer epitaxially grown on the graphone substrate, whose C1 is saturated by hydrogen and C2 is not. We find that in the optimized ground state, both In atoms in the simulation supercell are chemically bonded with graphone C atoms. In particular, one In is on the top site of the C1 atom while the other is on the C2 atom. The binding energy between the  $h$ -In monolayer and the graphone substrate is calculated to be  $E_b (= E_{h\text{-In}} + E_{\text{graphone}} - E_{h\text{-In@graphone}}) = 2.56$  eV per simulation supercell, confirming chemical bonding between In and C atoms. Relative energies for other absorbed patterns are given in Figure S1 of Supplemental Material [21]. In the ground state, due to the two inequivalent In atoms in the supercell, the  $h$ -In monolayer is not flat. The In atom bonded with the C1 is lower in height by 0.39 Å than the one located above C2. This corresponds to a staggered on-site potential for  $h$ -In monolayer which could lead to contrasting valley properties. Our phonon dispersion calculations show no imaginary frequencies [Fig. 1(b)] which confirm its dynamical stability. Note that group-IIIA element based honeycomb sheets are not dynamically stable in their freestanding state as they are inconsistent with the aromatic rule. However, graphone works as a support to stabilize it. No gap is observed between the acoustic and optical branches.

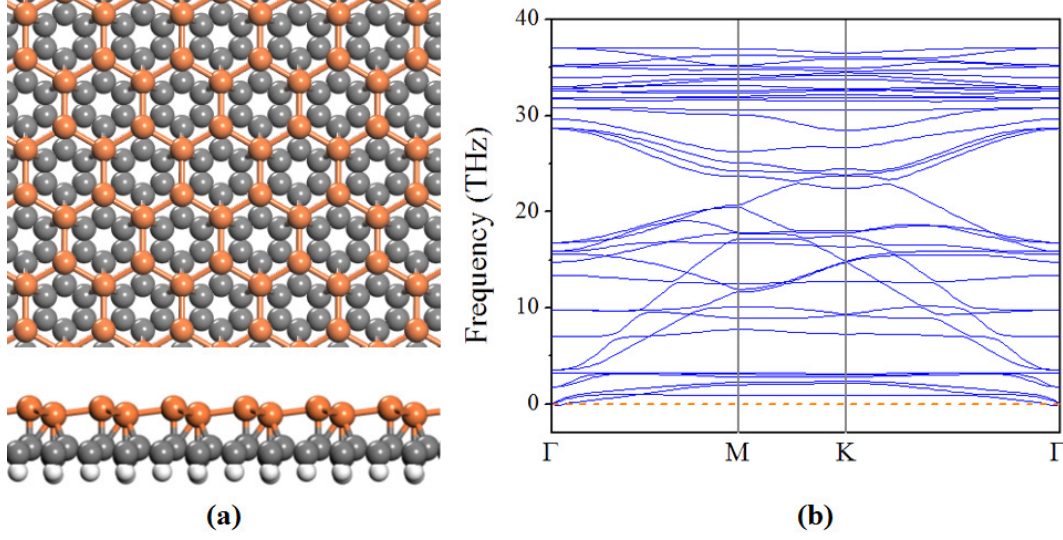


FIG. 1. (a) Structure (top view and side view) and (b) phonon dispersion of an epitaxial  $h$ -In monolayer grown on graphone. Orange, gray, and white spheres in (a) represent In, C, and H atoms, respectively.

### C. Electronic structure with and without spin-orbit coupling

Next we calculated the electronic properties of the epitaxial  $h$ -In monolayer supported on graphone. Consistent with our above electron counting analysis, the electrons from In atoms form  $\sigma$  bonds with the C- $p_z$  electrons, so that magnetism of graphone is totally quenched. Figure 2(a) shows our calculated band structure without including SOC interaction. We use blue circles to represent states projected onto In- $p_z$  orbitals, with their radii proportional to percentage contribution from In- $p_z$  orbitals. We see that both valence band ( $\pi$  character) and conduction band ( $\pi^*$  character) are doubly degenerate in spin up and spin down channels and are mainly composed of In- $p_z$  electrons (with a small portion of C- $p_z$  due to their  $\sigma$  bonding). Besides, a direct band gap of  $\Delta = 46$  meV at  $K$  (and  $K'$ ) point of the BZ is formed. This nonzero finite band gap is due to breaking of quasi-2D inversion symmetry [11] of the  $h$ -In layer. Note that the frontier bands are located inside the band gap of graphone substrate. Next, we turn on the SOC interaction. Due to the lack of inversion symmetry, SOC shows Rashba character, which is sketched in the inset of Fig. 2(a). The doubly degenerate valence and conduction bands split into two bands (referred to as VB-1, VB; and CB, CB+1). Here the indices VB-1 and VB denote the

$N-1^{\text{th}}$  and  $N^{\text{th}}$  bands at each  $k$ -point, respectively, where  $N$  is the total number of electrons in the simulation supercell. The CB and CB+1 correspond to the  $N+1^{\text{th}}$  and  $N+2^{\text{th}}$  bands, respectively. Hence, at each valley,  $E_{\text{VB}-1} < E_{\text{VB}} < E_{\text{CB}} < E_{\text{CB}+1}$ . As shown in Fig. 2(b), for the CB and CB+1, the  $E_{\text{CB},K}$  is energetically lower than  $E_{\text{CB}+1,K}$  by 5.5 meV. Here, we use  $E_{n,\mathbf{k}}$  to denote the eigenvalue of the  $n$ -th band at the  $\mathbf{k}$  point of the BZ. On the other hand, the  $E_{\text{VB},K}$  is higher in energy than  $E_{\text{VB}-1,K}$  by 20 meV. Hence, after including SOC interaction, the global band gap of the system decreases to 35 meV which can be observed at room temperature. Note that such Rashba states are well situated inside the band gap of the substrate. This shows an “ideal” feature that can be detected and used as a strong modulation of spin-polarized current in spintronic transistor [15].

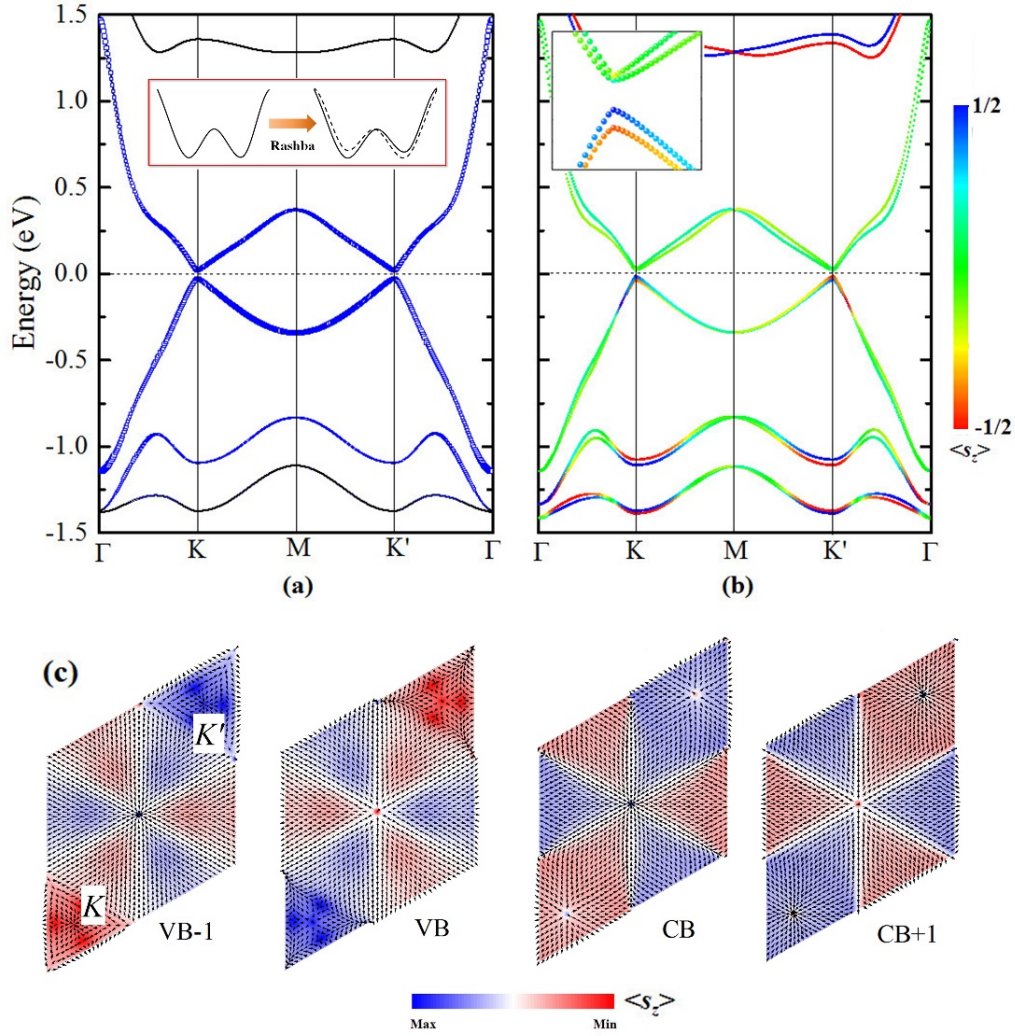




FIG. 2. Band structure (a) without and (b) with SOC interaction of  $h$ -In monolayer adsorbed on graphone. In (a) we use blue circles to represent In- $p_z$  orbital contributions of each state. The sketch of Rashba-type SOC induced band splitting is shown in the inset of (a). The color in (b) represents the  $\langle s_z \rangle$  of each state. Inset of (b) shows the zoom-in band dispersion around the K point. (c) The spin textures of VB-1, VB, CB, and CB+1 bands. The in-plane spin texture is shown as arrows, while the  $\langle s_z \rangle$  is shown by the background colors, with blue and red indicating spin up and spin down, respectively.

As it is well known that the PBE functional underestimates the band gaps, we use the HSE06 hybrid functional [22, 23] to verify the computed band structure. Compared with PBE results, the band structures calculated by HSE06 shift away from the Fermi level, while keeping their main dispersive profiles (Fig. S2 in Ref. [21]). The direct band gap (without SOC) between the valence and conduction bands is increased to 176 meV. When SOC is included, we again see obvious Rashba splitting, and the band gap between the VB and CB at K ( $K'$ ) point is 107 meV, which is sufficiently large to be observed and used at room temperature. The energy difference between VB-1 and VB at K is 40 meV, and that between CB and CB+1 is 37 meV.

We also calculate the spin texture of these bands  $\langle \mathbf{s}_{nk} \rangle = [\langle s_{x,nk} \rangle, \langle s_{y,nk} \rangle, \langle s_{z,nk} \rangle]$ , where  $\langle s_{i,nk} \rangle = \langle \psi_{nk} | \sigma_i / 2 | \psi_{nk} \rangle$  ( $i = x, y, z$ , and  $\sigma_i$  is the Pauli matrix). As shown in Fig. 2(c), one clearly sees that the spin texture shows opposite values between VB and VB-1, and between CB and CB+1, due to time-reversal symmetry. In particular, the  $\langle s_z \rangle$  of VB at  $K$  is positive (spin down), while it is negative (spin up) at  $K'$  point. For the CB, the  $\langle s_z \rangle$  shows positive and negative value at  $K$  and  $K'$ , respectively. It becomes flat (only in-plane component) and flips its sign in the vicinity of  $K$  and  $K'$ . The in-plane spin texture ( $s_x, s_y$ ) of these bands are plotted as arrows. We observe that in the CB (CB+1), the in-plane spin texture around both  $K$  and  $K'$  are pointing radically outward (inward), making both  $K$  and  $K'$  serve as sources (sinks) of in-plane “spin flow”. This corresponds to a hedgehog skyrmion [24, 25] spin texture pair at  $K$  and  $K'$  as can be clearly observed in a zoom-in texture (Fig. S3 in Ref. [21]). As far as we know, this skyrmion pair in the conduction bands of  $p$ -electron based honeycomb lattice has not been observed before. By calculating the topological charge for each valley,  $n = 1/4\pi \times \int \mathbf{M} \cdot (\partial_x \mathbf{M} \times \partial_y \mathbf{M}) dk^2$  where  $\mathbf{M}$  is unit vector in the direction of spin texture, we obtain  $n_K = -n_{K'} = 1$ . This yields a topologically trivial

character of the whole CB (and CB+1), but for each valley the topological index is nonzero. The in-plane spin texture for VB (VB-1) around both  $K$  and  $K'$  are pointing outward (inward).

#### D. Valley selective circular polarization adsorption

The opposite behaviors of the two valleys imply an electronic valley contrasting character. One important application of such valley contrasting system is its optical selectivity of valleys which is measured by the degree of circular polarization [1],

$$\eta(\mathbf{k}) = \frac{|P_+(\mathbf{k})|^2 - |P_-(\mathbf{k})|^2}{|P_+(\mathbf{k})|^2 + |P_-(\mathbf{k})|^2},$$

where  $P_{\pm}(\mathbf{k})$  is inter-band matrix element of absorption of left-(+) and right-(-) handed polarized luminescence between the VB and CB. It is evaluated as  $P_{\pm}(\mathbf{k}) = \langle \psi_{CB,\mathbf{k}} | p_x \pm i p_y | \psi_{VB,\mathbf{k}} \rangle$ , where  $p_x$  and  $p_y$  are momentum operators. The calculated degree of circular polarization is plotted in Fig. 3(a), where we see that  $\eta(\mathbf{k})$  has a  $C_3$  rotation symmetry in the whole 2D BZ, consistent with the crystalline symmetry of the system. In particular, at the direct band gap position,  $\eta(K) = +1$  and  $\eta(K') = -1$ . This suggests a perfect left-handed and right-handed valley selective absorption which originates from the lack of inversion symmetry in the structure. Such valley selection feature has also been verified by using HSE06+SOC method [21].

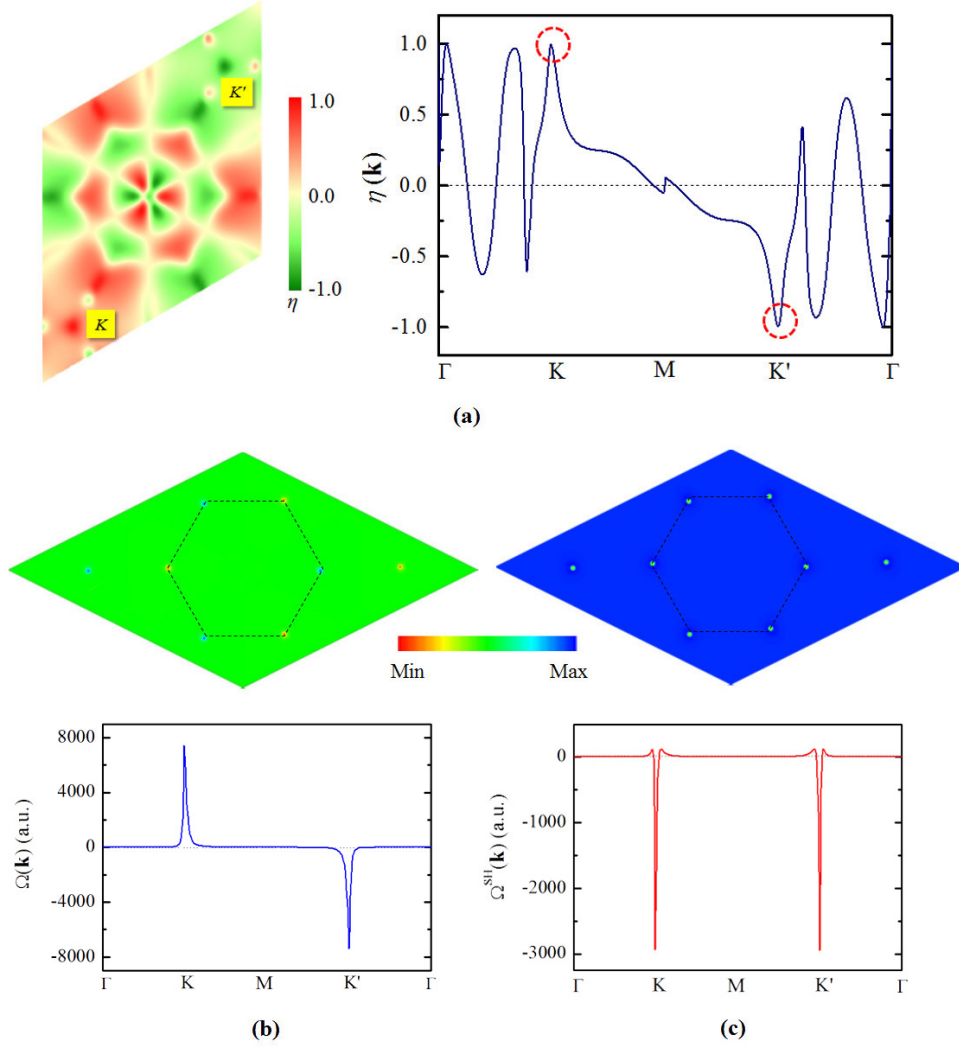


FIG. 3. (a) The  $k$ -resolved degree of circular polarization  $\eta(\mathbf{k})$  in the whole BZ (left) and along the high symmetry  $k$ -paths (right). (b) Berry curvature and (c) spin Berry curvature of  $h$ -In adsorbed on graphene; in the whole BZ (up panel) and along the high symmetry  $k$ -paths (down panel).

### E. Berry curvatures and anomalous Nernst conductance

We then calculate the Berry curvature  $\Omega(\mathbf{k})$  and spin Berry curvature  $\Omega^S(\mathbf{k})$  by using the Kubo formula [26,27],

$$\Omega(\mathbf{k}) = \sum_{E_{n,\mathbf{k}} \leq \mu} \sum_{n' \neq n} \frac{-2 \text{Im} \langle \psi_{n,\mathbf{k}} | \hat{v}_x | \psi_{n',\mathbf{k}} \rangle \langle \psi_{n',\mathbf{k}} | \hat{v}_y | \psi_{n,\mathbf{k}} \rangle}{(E_{n\mathbf{k}} - E_{n'\mathbf{k}})^2}$$

$$\Omega^S(\mathbf{k}) = \sum_{E_{n,\mathbf{k}} \leq \mu} \sum_{n' \neq n} \frac{-2 \text{Im} \langle \psi_{n,\mathbf{k}} | \hat{j}_x | \psi_{n',\mathbf{k}} \rangle \langle \psi_{n',\mathbf{k}} | \hat{v}_y | \psi_{n,\mathbf{k}} \rangle}{(E_{n\mathbf{k}} - E_{n'\mathbf{k}})^2},$$

where  $\mu$  is the chemical potential and  $j_x$  is spin current operator defined as  $(v_x s_z + s_z v_x)/2$ . The results are plotted in Fig. 3(b) and 3(c). The  $\Omega(\mathbf{k})$  and  $\Omega^S(\mathbf{k})$  are odd and even functions, respectively, due to time reversal symmetry. We observe that both curvatures have pronounced peaks at the  $K$  and  $K'$  valleys. The odd function of  $\Omega(\mathbf{k})$  makes the total Chern number  $C = \int d^2\mathbf{k} \Omega(\mathbf{k})/2\pi = 0$ . On the other hand, the  $\Omega^S(K)$  and  $\Omega^S(K')$  are both negative. However, in the vicinity of  $K$  (and  $K'$ ) the  $\Omega^S(\mathbf{k})$  shows positive values. The integration of the  $\Omega^S(\mathbf{k})$  in the whole 2D BZ also gives a vanishing number,  $C^S = \int d^2\mathbf{k} \Omega^S(\mathbf{k})/2\pi = 0$ . This demonstrates that the band gap of  $h$ -In monolayer adsorbed on graphone has a trivial topology, similar to that in  $H$ -MoS<sub>2</sub> monolayer [28]. We also calculated the  $\Omega(\mathbf{k})$  and  $\Omega^S(\mathbf{k})$  along the high symmetry  $k$ -path by using HSE06+SOC method, and consistent results are obtained [21]. The HSE06+SOC calculated  $\Omega(\mathbf{k})$  and  $\Omega^S(\mathbf{k})$  have relatively lower peak at the valleys, due to the larger band gap. However, one can see that the peak widths of  $\Omega(\mathbf{k})$  and  $\Omega^S(\mathbf{k})$  also become larger, hence the integration over the whole BZ would remain the same.

Very recently, Yu *et al.* predicted that  $H$ -MoS<sub>2</sub> and other TMD monolayers have a spin and valley dependent anomalous Nernst effect [29]. Due to the Seebeck effect, a built-in electric field develops in the opposite direction when the system is immersed in a temperature gradient. Hence the electron moves under such an electric field. Simultaneously, movements in the transverse direction appear under Lorentz-like force. This is termed as anomalous Nernst effect and has been formulated in the language of Berry phases as a momentum space geometric effect [29]. Motivated by this, we calculated the anomalous Nernst coefficient (ANC) and spin Nernst coefficient (SNC) of the two valleys by separately integrating Berry curvatures,

$$\text{ANC}^{K,K'} = 2\alpha_0 \int_{K,K'} \frac{d^2\mathbf{k}}{2\pi} \Omega(\mathbf{k}) S(\mathbf{k}) = \alpha_{\uparrow}^{K,K'} + \alpha_{\downarrow}^{K,K'}$$

$$\text{SNC}^{K,K'} = 2\alpha_0 \int_{K,K'} \frac{d^2\mathbf{k}}{2\pi} \Omega^S(\mathbf{k}) S(\mathbf{k}) = \frac{1}{2} (\alpha_{\uparrow}^{K,K'} - \alpha_{\downarrow}^{K,K'})$$

where  $\alpha_0 = ek_B/2h$ ,  $S(\mathbf{k}) = -f_{n,\mathbf{k}}\ln f_{n,\mathbf{k}} - (1 - f_{n,\mathbf{k}})\ln(1 - f_{n,\mathbf{k}})$  is the entropy density and  $f_{n,\mathbf{k}}$  is Fermi-Dirac occupation. Here, a factor of  $2e/\hbar$  has been multiplied in  $\Omega^S(\mathbf{k})$  in order to convert the SNC unit the same as ANC.  $\alpha_\uparrow$  and  $\alpha_\downarrow$  are spin resolved anomalous Nernst coefficients at each valley. The integrations are carried out in a triangular region centered at  $K$  (and  $K'$ ) valley and its area equals to half of the first BZ. In Figure 4(a) we show the chemical potential dependent ANC and SNC for the  $K$  valley at room temperature, namely, 300 K. The ANC at  $K$  is positive (negative) when the chemical potential is moved to higher (lower) energy range from the Fermi level ( $E_F$ ), while it vanishes at the Fermi level. The dominant positive (negative) peak lies at  $\mu = 0.05$  eV ( $-0.05$  eV), with value of around  $0.2\alpha_0$  ( $-0.14\alpha_0$ ). The calculated SNC curves show a positive peak of  $\sim 0.2\alpha_0$  at  $\mu = -0.2$  eV. At the intrinsic condition ( $\mu = 0$ ), the SNC is negative with the value of about  $-0.1\alpha_0$ . Such nonzero value is due to the small band gap of the system, so that both valence and conduction bands contribute to the calculated SNC. Due to the odd and even features of  $\Omega(\mathbf{k})$  and  $\Omega^S(\mathbf{k})$ , the ANC for the  $K'$  valley is opposite to that for the  $K$  valley, and the SNC for the  $K'$  is the same as that for the  $K$ . This has been confirmed through DFT-GGA calculation. Note that for each valley  $\alpha_\uparrow^{K,K'} = (\text{ANC}^{K,K'} + 2 \times \text{SNC}^{K,K'})/2$  and  $\alpha_\downarrow^{K,K'} = (\text{ANC}^{K,K'} - 2 \times \text{SNC}^{K,K'})/2$  [Fig. 4(b)]. We find  $\alpha_\uparrow^{K,K'} \sim -\alpha_\downarrow^{K,K'}$  which is due to time reversal symmetry and is consistent with previous results for  $H\text{-MoS}_2$  monolayer [29]. For the anomalous Nernst current, the spin current purity factor (SCPF) is defined as

$$\text{SCPF} = \frac{(\alpha_\uparrow^K + \alpha_\uparrow^{K'}) - (\alpha_\downarrow^K + \alpha_\downarrow^{K'})}{|\alpha_\uparrow^K| + |\alpha_\uparrow^{K'}| + |\alpha_\downarrow^K| + |\alpha_\downarrow^{K'}|},$$

which takes value between  $-1$  and  $+1$ . As seen in Fig. 4(c), the SCPF shows a  $\sim 70$  meV wide terrace with value of  $-1$  when  $\mu$  is located around the  $E_F$ , while it increases continuously to  $+1$  as  $\mu$  is tuned away from the  $E_F$ . This is different from the case of  $H\text{-MoS}_2$  where the SCPF is  $+1$  when the  $\mu$  is tuned between the VB-1 and VB and is ill-defined around the Fermi level.

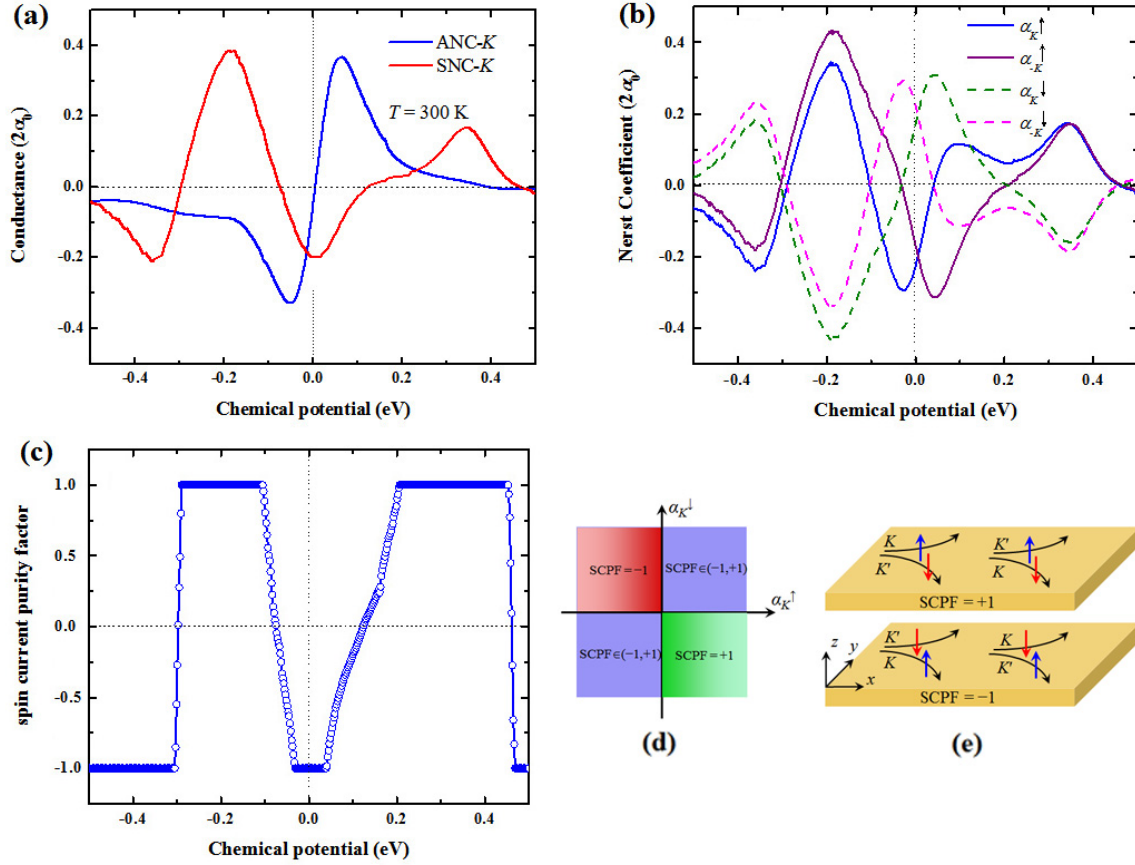


FIG. 4. ANC and SNC as a function of chemical potential at 300 K around the (a)  $K$  valley. The chemical potential dependent (b) spin resolved ANC for each valley and (c) SCPF. The zero chemical potential represents the Fermi level. (d) is the phase diagram for spin current purity factor, and (e) shows the spin current in different valleys when the SCPF is quantized.

The physical meaning of quantized terraces of SCPF can be understood by analyzing the spin resolved anomalous Nernst coefficients. Since  $\alpha_\uparrow^{K,K'} = -\alpha_\downarrow^{K',K}$ ,  $\text{SCPF} = (\alpha_\uparrow^K - \alpha_\downarrow^K) / (|\alpha_\uparrow^K| + |\alpha_\downarrow^K|)$ . There are four cases that lead SCPF to be  $\pm 1$ : (i)  $\alpha_\uparrow^K \neq 0$  and  $\alpha_\downarrow^K = 0$ ,  $\text{SCPF} = \text{sgn}(\alpha_\uparrow^K)$ ; (ii)  $\alpha_\uparrow^K = 0$  and  $\alpha_\downarrow^K \neq 0$ ,  $\text{SCPF} = -\text{sgn}(\alpha_\downarrow^K)$ ; (iii)  $\alpha_\uparrow^K > 0$  and  $\alpha_\downarrow^K < 0$ ,  $\text{SCPF} = +1$ ; (iv)  $\alpha_\uparrow^K < 0$  and  $\alpha_\downarrow^K > 0$ ,  $\text{SCPF} = -1$ . When the  $\alpha_\uparrow^K \times \alpha_\downarrow^K > 0$ , the SCPF is within the range of  $(-1, 1)$ , indicating mixed spin current. When the  $\alpha_\uparrow^K = \alpha_\downarrow^K = 0$ , the SCPF is ill-defined. The phase diagram is shown in Fig. 4(d). Thus, the  $\text{SCPF} = +1$  ( $-1$ ) indicates that the spin up current is moving along the positive (negative)  $y$  direction, while the spin down current is moving along

the negative (positive)  $y$  direction, when the temperature gradient is in the  $x$  direction [Fig. 4(e)]. Hence, in our proposed  $h$ -In adsorbed graphone, one is able to obtain pure spin current induced by thermal gradient at its neutral state.

We also calculate the ANC and SNC at different temperatures (Fig. S4 in Ref. [21]). The ANC curves at  $K$  valley have similar features – they all show a positive (negative) peak when  $\mu > 0$  ( $< 0$ ). As the temperature decreases to 100 K, the peak width becomes narrow, while the height of the peak almost remains at similar level. However, for SNC, one observes that at lower temperature its peak magnitude becomes smaller, and vanishes at very low temperature.

### F. Substrate thickness effect

We now consider the effect of the substrate thickness. We use a semi-hydrogenated (the bottom C atoms saturated) diamond (111) thin film as substrate to support  $h$ -In monolayer. Figure 5 summarizes the band energy variations with respect to number of C layers ( $n$ ) of the thin film, calculated using the PBE functional. SOC interaction has been included. We see that as  $n$  increases, the system remains semiconducting and the global band gap gradually increases. The calculated  $E_g$  ( $= E_{CB,K} - E_{VB,K}$ ) becomes 57 meV when  $n = 4$ . The Rashba splitting in valence and conduction bands show different behavior. As the number of layers increases, we observe that the energy difference between CB+1 and CB at  $K$  valley is also increased (from 6 meV for  $n = 1$  to 10 meV for  $n = 4$ ), while the energy difference between VB and VB-1 decreases from 20 meV for  $n = 1$  to 7 meV for  $n = 4$ . We have calculated band gap variations with respect to the layer number by using HSE06+SOC method, and the results are summarized in Fig. S5 [21]. We still can observe clear Rashba splitting in all cases. In particular, the  $E_g$  increases from 107 meV for  $n = 1$  to 938 meV for  $n = 3$ . This confirms that the substrate thickness is an effective parameter to tune the band gaps, and the corresponding valley properties also can be manipulated.

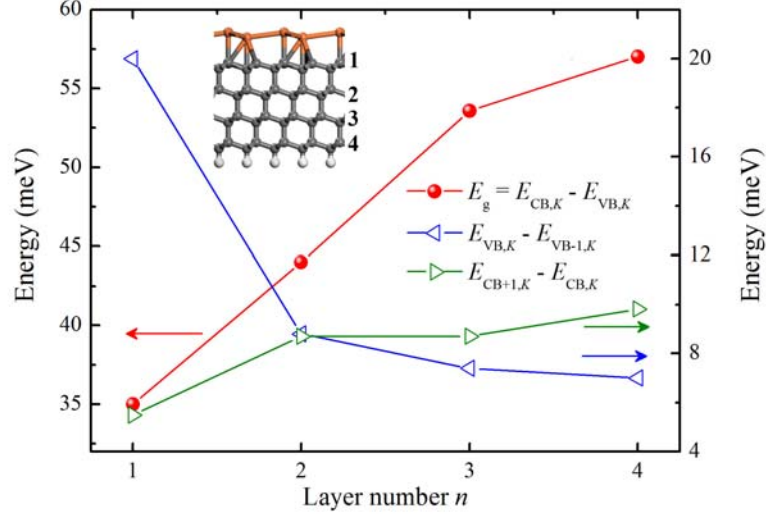


FIG. 5. Layer number dependence of energy gap and SOC band energy splitting at the K valley. Inset shows the  $h$ -In monolayer adsorbed on a semi-hydrogenated diamond (111) thin film with four C layers.

### H. Honeycomb Tl adsorption

Before concluding, we briefly discuss  $h$ -Tl monolayer epitaxial growth on graphone. The band structure is shown in Fig. S6 [21]. The system shows a similar direct band gap semiconducting feature. Both valence and conduction bands are contributed by Tl- $p_z$  electrons which are well located in the bulk band gap of the graphone substrate. The band gap calculated without including SOC interaction is 54 meV. The SOC interaction lifts the degeneracy of valence and conduction bands and narrows the band gap. Because Tl is heavier than In, the SOC effect in  $h$ -Tl is stronger than that in  $h$ -In monolayer. Hence, we observe larger Rashba-type band splitting than that in  $h$ -In case. The calculated  $E_{VB,K} - E_{VB-1,K}$  and  $E_{CB+1,K} - E_{CB,K}$  are 54 meV and 35 meV, respectively, and the band gap  $E_g$  ( $= E_{CB,K} - E_{VB,K}$ ) becomes 11 meV. This also provides an opportunity to realize ideal Rashba bands in reality in future spintronic applications.



#### IV. Conclusion

In conclusion, using density functional theory, we predict a dynamically stable honeycomb In/Tl monolayer which can be epitaxially grown on a semi-hydrogenated graphene (or diamond) surface. The two In (or Tl) atoms in one supercell reside on different sites of graphone, hence the system shows a direct band gap at  $K$  and  $K'$  valleys. Both valence and conduction bands are mainly contributed by In/Tl- $p_z$  orbitals. Due to the lack of inversion symmetry, two valleys are inequivalent. After including SOC interaction, the valence and conduction bands show strong Rashba type splitting. Hedgehog skyrmion spin texture features are observed in the split conduction bands at  $K$  and  $K'$  valleys. This provides a realizable material to have staggered on-site potential of  $p$ -electron honeycomb lattice, proposed in previous model calculations. Due to strong SOC interactions,  $h$ -In/Tl on graphone exhibits a perfect valley contrasting circular polarization light absorption behavior. By integrating its (spin) Berry curvatures, we reveal that such structures possess large Nernst anomalous conductivity, as well as pure spin current.

**Acknowledgments.** This work is supported by grants from the U.S. Department of Energy, Office of Basic Energy Sciences, Division of Materials Sciences and Engineering (# DE-FG02-96ER45579 and DE-FG02-11ER46827). C.H. acknowledges the China Scholarship Council for sponsoring his visit to Virginia Commonwealth University where this work was conducted. This material is based upon work performed using computational resources supported by the University of Tennessee and Oak Ridge National Laboratory's Joint Institute for Computational Sciences (<http://www.jics.utk.edu>) [30]. Any opinions, findings, and conclusions or recommendations expressed in this material are those of the author(s) and do not necessarily reflect the views of the University of Tennessee, Oak Ridge National Laboratory, or the Joint Institute for Computational Sciences. E. K. was supported by the NSFC (21203096, 51522206), by NSF of Jiangsu Province (BK20130031), by PAPD, the Fundamental Research Funds for the Central Universities (No.30915011203), by New Century Excellent Talents in University (NCET-12-0628).

## Reference:

- [1] T. Cao, G. Wang, W. Han, H. Ye, C. Zhu, J. Shi, Q. Niu, P. Tan, E. Wang, B. Liu, and J. Feng, Valley-Selective Circular Dichroism of Monolayer Molybdenum Disulphide. *Nat. Commun.* **3**, 887 (2012).
- [2] K. Mak, K. He, J. Shan, and T. F. Heinz, Control of Valley Polarization in Monolayer  $\text{MoS}_2$  by Optical Helicity. *Nat. Nanotechnol.* **7**, 494 (2012).
- [3] D. Xiao, G.-B. Liu, W. Feng, X. Xu, and W. Yao, Coupled Spin and Valley Physics in Monolayers of  $\text{MoS}_2$  and Other Group-VI Dichalcogenides. *Phys. Rev. Lett.* **108**, 196802 (2012).
- [4] Q. Liu, X. Zhang, and A. Zunger, Intrinsic Circular Polarization in Centrosymmetric Stacks of Transition-Metal Dichalcogenide Compounds. *Phys. Rev. Lett.* **114**, 087402 (2015).
- [5] D. Xiao, W. Yao, and Q. Niu, Valley-Contrasting Physics in Graphene: Magnetic Moment and Topological Transport. *Phys. Rev. Lett.* **99**, 236809 (2007).
- [6] A. Rycerz, J. Tworzydło, and C. W. J. Beenakker, Valley filter and valley valve in graphene. *Nat. Phys.* **3**, 172 (2007).
- [7] W. Yao, S. A. Yang, and Q. Niu, Edge States in Graphene: From Gapped Flat-Band to Gapless Chiral Modes. *Phys. Rev. Lett.* **102**, 096801 (2009).
- [8] F. Zhang, A. H. MacDonald, and E. J. Mele, Valley Chern numbers and boundary modes in gapped bilayer graphene. *Proc. Natl. Acad. Sci. U.S.A.* **110**, 10546 (2013).
- [9] A. Vaezi, Y. Liang, D. H. Ngai, L. Yang, and E.-A. Kim, Topological Edge States at a Tilt Boundary in Gated Multilayer Graphene. *Phys. Rev. X* **3**, 021018 (2013).
- [10] L. Ju, Z. Shi, N. Nair, Y. Lv, C. Jin, J. Velasco Jr, C. Ojeda-Aristizabal, H. A. Bechtel, M. C. Martin, A. Zettl, J. Analytis, and F. Wang, Topological valley transport at bilayer graphene domain walls. *Nature* **520**, 650 (2015).
- [11] Y. Li, D. West, H. Huang, J. Li, S. B. Zhang, and W. Duan, Theory of the Dirac half metal and quantum anomalous Hall effect in Mn-intercalated epitaxial graphene. *Phys. Rev. B* **92**, 201403(R) (2015).

- [12] J. Zhou, Q. Wang, Q. Sun, X. S. Chen, Y. Kawazoe, and P. Jena, Ferromagnetism in Semihydrogenated Graphene Sheet. *Nano Lett.* **9**, 3867 (2009).
- [13] J. Zhou and Q. Sun, How to fabricate a semihydrogenated graphene sheet? A promising strategy explored. *Appl. Phys. Lett.* **101**, 073114 (2012).
- [14] R. Balog, B. Jørgensen, L. Nilsson, M. Andersen, E. Rienks, M. Bianchi, M. Fanetti, E. Lægsgaard, A. Baraldi, S. Lizzit, Z. Sljivancanin, F. Besenbacher, B. Hammer, T. G. Pedersen, P. Hofmann, and L. Hornekær, Bandgap opening in graphene induced by patterned hydrogen adsorption. *Nature Mater.* **9**, 315 (2010).
- [15] W. Ming, Z. F. Wang, M. Zhou, M. Yoon, and F. Liu, Formation of Ideal Rashba States on Layered Semiconductor Surfaces Steered by Strain Engineering. *Nano Lett.* **16**, 404 (2016).
- [16] G. Kresse and J. Furthmüller, Efficient Iterative Schemes for Ab Initio Total-Energy Calculations Using a Plane-Wave Basis Set. *Phys. Rev. B* **54**, 11169 (1996).
- [17] J. P. Perdew, K. Burke, and M. Ernzerhof, Generalized Gradient Approximation Made Simple. *Phys. Rev. Lett.* **77**, 3865 (1996).
- [18] P. E. Blochl, Projector Augmented-Wave Method. *Phys. Rev. B* **50**, 17953 (1994).
- [19] H. J. Monkhorst and J. D. Pack, Special Points for Brillouin-Zone Integrations. *Phys. Rev. B* **13**, 5188 (1976).
- [20] A. Togo, F. Oba, and I. Tanaka, First-principles calculations of the ferroelastic transition between rutile-type and  $\text{CaCl}_2$ -type  $\text{SiO}_2$  at high pressures. *Phys. Rev. B* **78**, 134106 (2008).
- [21] Supplemental Material for relative energies of  $h$ -In on graphone, spin texture, band properties calculated by HSE06 functional, ANC and SNC at different temperature, and band structure of  $h$ -Tl on graphone.
- [22] J. Heyd, G. E. Scuseria, and M. Ernzerhof, Hybrid Functionals Based on a Screened Coulomb Potential. *J. Chem. Phys.* **118**, 8207 (2003).

[23] J. Heyd, G. E. Scuseria, and M. Ernzerhof, Erratum: “Hybrid Functionals Based on a Screened Coulomb Potential” [J. Chem. Phys. 118, 8207 (2003)]. J. Chem. Phys. **124**, 219906 (2006).

[24] M. Ezawa, Compact merons and skyrmions in thin chiral magnetic films. Phys. Rev. B **83**, 100408(R) (2011).

[25] A. Petković and M. V. Milovanović, Fractionalization into Merons in Quantum Dots. Phys. Rev. Lett. **98**, 066808 (2007).

[26] Y. G. Yao, L. Kleinman, A. H. MacDonald, J. Sinova, T. Jungwirth, D.-S. Wang, E. Wang, and Q. Niu, First Principles Calculation of Anomalous Hall Conductivity in Ferromagnetic bcc Fe. Phys. Rev. Lett. **92**, 037204 (2004).

[27] Y. G. Yao and Z. Fang, Sign Changes of Intrinsic Spin Hall Effect in Semiconductors and Simple Metals: First-Principles Calculations. Phys. Rev. Lett. **95**, 156601 (2005).

[28] W. Feng, Y. Yao, W. Zhu, J. Zhou, W. Yao, and D. Xiao. Intrinsic spin Hall effect in monolayers of group-VI dichalcogenides: A first-principles study. Phys. Rev. B **86**, 165108 (2012).

[29] X.-Q. Yu, Z.-G. Zhu, G. Su, and A.-P. Jauho, Thermally Driven Pure Spin and Valley Currents via the Anomalous Nernst Effect in Monolayer Group-VI Dichalcogenides. Phys. Rev. Lett. **115**, 246601 (2015).

[30] M. R. Fahey, R. Budiardja, L. Crosby, and S. McNally, “Deploying Darter – A Cray XC30 System,” Lecture Notes in Computer Science, J. M. Kunkel, T. Ludwig, and H.W. Meuer (Eds.): ISC 2014, LNCS 8488, pp. 430–439, Springer International Publishing Switzerland June 2014.